



Lung nodule segmentation and recognition using SVM classifier and active contour modeling: A complete intelligent system



Mohsen Keshani, Zohreh Azimifar*, Farshad Tajeripour, Reza Boostani

Department of Computer Science and Engineering, School of Electrical and Computer Engineering, Shiraz University, Shiraz, Iran

ARTICLE INFO

Article history:

Received 6 July 2011

Accepted 9 December 2012

Keywords:

Lung nodules

Detection

Segmentation

Connectivity recognition

Active contour

SVM classifier

ABSTRACT

In this paper, a novel method for lung nodule detection, segmentation and recognition using computed tomography (CT) images is presented. Our contribution consists of several steps. First, the lung area is segmented by active contour modeling followed by some masking techniques to transfer non-isolated nodules into isolated ones. Then, nodules are detected by the support vector machine (SVM) classifier using efficient 2D stochastic and 3D anatomical features. Contours of detected nodules are then extracted by active contour modeling. In this step all solid and cavitory nodules are accurately segmented. Finally, lung tissues are classified into four classes: namely lung wall, parenchyma, bronchioles and nodules. This classification helps us to distinguish a nodule connected to the lung wall and/or bronchioles (attached nodule) from the one covered by parenchyma (solitary nodule). At the end, performance of our proposed method is examined and compared with other efficient methods through experiments using clinical CT images and two groups of public datasets from Lung Image Database Consortium (LIDC) and ANODE09. Solid, non-solid and cavitory nodules are detected with an overall detection rate of 89%; the number of false positive is 7.3/scan and the location of all detected nodules are recognized correctly.

© 2012 Elsevier Ltd. All rights reserved.

1. Introduction

Lung cancer is the deadliest cancer for men and the second deadliest cancer for women globally [1]. For instance, about 219,000 lung cancer cases are diagnosed in the US each year [2]. The specific abnormality that indicates lung cancer is growth of a nodule in the lung area. There are some different clinical nodule parameters that guide the radiologist in making a diagnosis of lung cancer. The first indicator is the shape of the nodule. A jagged shape nodule seems more likely to be lung cancer than a smoothed one. The second parameter is the texture of the nodule. If it is fatty, bony, watery or a mixture of different contents, the level of suspicion for lung cancer would be different. The third parameter is the location of the nodule. For instance, solitary nodules seem less likely to be lung cancer than vessel attached ones [3]. The growth rate of the volume of nodule is the fourth affecting parameter. For example, lung wall or fissure attached nodules typically are benign with volume-doubling period longer than 400 days.

Irregular shapes, complicated anatomical locations and sometimes low intensities of nodules lead to some problems for manual

detection, segmentation, recognition and volumetric processes. Performing these processes manually is highly difficult, time consuming, and inaccurate. Having considered these issues, a complete system is required to perform these processes automatically.

1.1. Previous work

In recent years, various methods have been proposed for lung segmentation and nodule detection and also a few algorithms have been proposed for nodule segmentation and recognition. A number of lung segmentation algorithms perform very well but with some limitation in detecting non-isolated nodules connected to the chest walls [4,5]. In addition, there are nodule detection algorithms with good performance for only detecting solid pulmonary lesions [6]. Although some detecting algorithms are useful for solid nodules, their performance for detecting cavitory nodules is poor [7]. Only a few methods include segmentation with or without nodule recognition [8,9], some classify nodules based on their spatial locations [3,10] and some perform classification based on nodule texture and shape [11].

Ye et al. [7] proposed a shape-based computer-aided detection (CAD) of lung nodules acquired by CT scans. To obtain the initial lung mask, 3D adaptive fuzzy thresholding was applied. The authors used chain code to estimate the complete lung mask. In their lung segmentation algorithm, small nodules attached to the lung wall were detected correctly as a part of the lung area

* Corresponding author. Tel.: +98 917 336 0805.

E-mail addresses: keshani.mhsn@yahoo.com (M. Keshani), azimifar@cse.shirazu.ac.ir (Z. Azimifar), tajeri@shirazu.ac.ir (F. Tajeripour), boostani@shirazu.ac.ir (R. Boostani).

by applying chain code. This method fails in detecting large sized non-isolated nodules connected to the chest wall, because these kinds of nodules seem to be a part of the chest wall after applying 3D adaptive fuzzy thresholding on CT lung images. In the nodule detection method of [7], 2D and 3D features were calculated to detect solid and GGO (ground glass opacity: part solid and non-solid) nodules. Also, segmentation of potential nodules was done by adaptive thresholding and modified expectation maximization (MEM) methods. Support vector machine (SVM) classifier was utilized to reduce the number of false positive (FP) objects by removing non-nodule parts. In this classification, 15 features were used, including: intensity-based (mean, min, max, standard deviation, etc.), stochastic features (skewness and kurtosis), shape index, etc. This work achieved a detection rate of 94% for solid nodules and 88.2% for GGO nodules with FP value of 8.2/scan.

Shimoyama et al. [12] proposed an algorithm for lung segmentation to detect non-isolated nodules by active contour modeling. The authors took benefit of the fact that each slice in a CT data is similar to its previous slice. Accordingly, they used the lung mask of the current slice as the initial mask to implement the active contour on the next slice. Segmentation of the lung area in the initial slice was done by a simple masking technique which is useful for slices without non-isolated nodules. Although their method becomes problematic for thickened slices,¹ it could improve the number of true positive (TP) from 7 (without using their lung extraction algorithm) to 10 (with their lung extraction algorithm applied) by adding it in a CAD system. However, the number of FP was increased by about 5%.

In recent approaches, the nodule recognition process has been done for different purposes, such as degree of nodule malignancy, nodule locations, calcified or non-calcified nodules, etc. Taghavi Namin et al. [11] proposed an algorithm to detect nodules and to determine the degree of nodule malignancy by applying fuzzy *k*-nearest neighbor (F-KNN). The authors used geometric and intensity-based features to reflect the shape and size of nodules. These features are useful to classify potential nodules as non-nodule or nodule with different degrees of malignancy. In their method, nodules were recognized well, but contours of detected nodules were not extracted accurately. Some other nodule recognition methods focused on the location of nodules (effective to diagnose lung cancer). For example, Wu et al. [3] proposed a novel probability co-occurrence map to measure the spatial attachment/interaction between nodule and other structures for connectivity classification.

Generally, detecting non-isolated nodules (attached to the lung tissues), segmenting irregular shaped nodules and recognizing nodules with complicated anatomical locations are important issues of a CAD system of lung nodules. Although a number of approaches have contributed to detecting and segmenting different kinds of nodules, recognition and even accurate segmentation of nodules, which are important preprocess stages for segmentation of nodules, are still remaining as ongoing researches.

1.2. Our approach

In this paper, segmentation and recognition of lung nodules appearing in CT images are proposed. A block diagram of the proposed method is indicated in Fig. 1.

At first, the lung is segmented. Then, features of the lung area are extracted to classify it into two classes: nodules and non-nodules. After that, accurate contours of nodules are extracted by

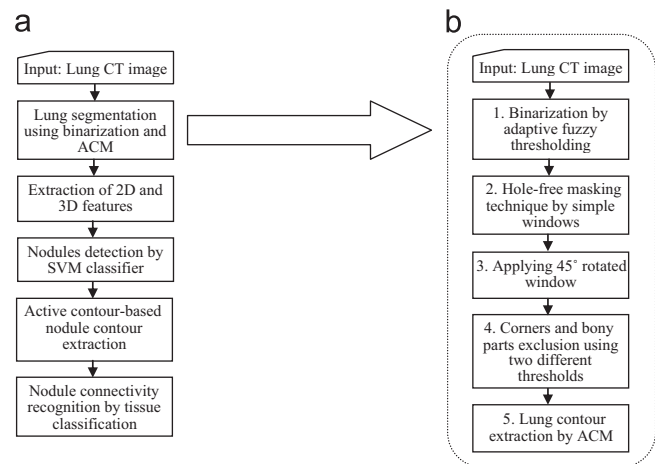


Fig. 1. (a) Block diagram of the proposed method. Lung CT images are the inputs of the algorithm, and the outputs are the segmented nodules and their locations; and (b) block diagram of proposed lung segmentation algorithm.

active contour modeling. Finally, by labeling different tissues of lung, nodules are recognized based on their locations, and whether they are attached or solitary. At the end, we propose a criterion to compare our method with other successful methods.

Different lung segmentation approaches are generally categorized into two different categories: first is known as histogram-based thresholding such as the one proposed in [7]. Using only this method for lung segmentation causes two problems. The first problem is coarse segmentation of lung area and the second problem is detection of nodules attached to the lung wall as a tissue outside the lung area. For solving the second problem, this thresholding requires some refinement processes to transfer non-isolated nodules to the isolated ones.

In the second category of lung segmentation, active contour models (ACMs) have been employed to extract contours of the lung accurately [5]. According to the structure of ACMs, they are sensitive to the external and internal energies. If a simple initialization (e.g. two auto-calculated circles around the lung areas [5]) is applied, non-isolated nodules will not be detected as a tissue inside the lung area. Thus, an appropriate initialization is necessary to accurately extract contours of lung area using ACM.

In this paper, by combining the above two basic methods, an automatic lung segmentation algorithm is proposed with a high degree of accuracy. In this way, an adaptive fuzzy thresholding [7] with some refinement processes is proposed for the initialization of an optimized active contour model. We use some masking techniques to transfer small and large non-isolated nodules connected to the chest wall to the isolated ones.

For nodule detection and segmentation, several algorithms have been proposed as were described in Section 1.1. We utilized 2D stochastic and 3D anatomical features in an SVM classifier to detect the nodules and to reduce the number of FP. Proposing an anatomical 3D feature leads to removing some segmental bronchus or bronchioles (small airways in the lung) which are not removed when only 2D features are considered. After the nodule detection step, initial contours of the nodules are used as the initialization of the active contour model (applying on the original image) to segment it with high precision.

One of the important parameters to determine the level of suspicion for lung cancer is to recognize whether the nodule is attached to the tissue or not. In this paper, this attachment is recognized by classifying all tissues of the thorax (lung wall, bronchioles, parenchyma and nodules). By considering the label of pixels neighboring nodule pixels, the class of nodule is determined.

¹ The similarity between two sequential slices is decreased across high thicknesses.

The proposed method was verified and evaluated on four groups of datasets: the first and the second groups are totally eight clinical datasets of thoracic CT scans, the third group is five datasets from ANODE09 (<http://anode09.isi.uu.nl>) and the fourth group is 50 datasets provided by LIDC (Lung Image Database Consortium). The experimental results indicate high performance of our method with high accuracy of nodule segmentation and an overall detection rate of 89% and FP value of 7.3/scan.

This paper is organized as follows: in the next section all the details of our proposed method are explained. In Section 3, experimental results and tuning of the parameters are illustrated. In Section 4, we discuss the results of the proposed method and compare them with similar algorithms. Conclusion and some future remarks are presented in Section 5.

2. Methodology

This section presents a detailed description of our proposed lung recognition system. Our contribution is fourfold: first a lung segmentation algorithm using ACM with appropriate initialization is proposed, second an efficient method for nodule detection by utilizing the SVM classifier is devised, third an accurate nodule segmentation algorithm using active contour modeling is given and finally a nodule recognition method by classifying and labeling lung tissues is proposed. An overview of our algorithm is given in Fig. 1 and details of different stages are described in this section.

2.1. Lung segmentation

For detecting nodules in the lung area, accurate segmentation of the lung is a very important step. In some CT scans, there are non-isolated nodules attached to the chest wall which complicate the lung segmentation process. This problem has already been addressed for small non-isolated nodules by applying chain code [7]; however this is not enough for our application. In this section, our segmentation method of the lung is described with a solution for large and small non-isolated nodules. In the first step, binary lung CT images are achieved by an adaptive fuzzy thresholding [7]. Then, two windows of different sizes are applied to obtain a hole-free mask. The initial lung mask is then obtained by sweeping a rotated window (which is shown in Fig. 2) on the entire hole-free binary image. In this step large and small non-isolated nodules are transferred to isolated ones inside the lung area. Finally, this initial mask is used to implement the active contour model [13] automatically and to segment the lung area accurately. By applying a new algorithm with our primary implementation presented in [14], the performances of the first and last steps are improved. The block diagram of the proposed lung segmentation algorithm is given in Fig. 1b, and the rest of this section describes [in detail] all steps.



Fig. 2. The window (45° rotated square) which is used in the third step of our lung segmentation algorithm.

In the first step, a binarization method is done by adaptive fuzzy thresholding. A majority of the pixels in the lungs have much lower intensities than the pixels of chest walls. By applying the binarization method, these lower intensity pixels are assigned zero and the pixels of the wall parts are logically assigned one. This step is done by defining $T_{\text{high}}(i)$ and $M_{\text{high}}(i)$, being the cumulative histogram and first moment, respectively, starting from maximum intensity I_{max} in the image. Similarly $T_{\text{low}}(i)$ and $M_{\text{low}}(i)$ are defined to start from minimum intensity I_{min} . In this paper, a simple masking is first applied to exclude voxels outside the thorax in the image. The result of this masking is called I . Then, I_{max} and I_{min} are calculated on the image I . Therefore, $M_{\text{high}}(i)$ and $M_{\text{low}}(i)$ are defined as

$$M_{\text{high}}(i) = \sum_{k=i}^{I_{\text{max}}-1} kp(k), \quad 0 \leq i \leq I_{\text{max}}-1$$

$$M_{\text{low}}(i) = \sum_{k=0}^i kp(k), \quad 0 \leq i \leq I_{\text{max}}-1 \quad (1)$$

where $p(k)$ is the histogram value of gray level k and i is the gray level value under consideration. The gray level i divides the histogram into two regions. The mean values of the two regions are calculated as given in [7]:

$$\mu_{\text{low}}(i) = \frac{M_{\text{low}}(i)}{T_{\text{low}}(i)}, \quad \mu_{\text{high}}(i) = \frac{M_{\text{high}}(i)}{T_{\text{high}}(i)} \quad (2)$$

Now, let us define $m_i(t)$ to be the membership measurement at one of two regions determined by the gray level i for each gray level t . The membership measurement function can be defined as:

$$m_i(t) = \frac{1}{1 + (d(t, \mu_{\text{low}}(i), \mu_{\text{high}}(i)) / (I_{\text{max}} - 1))} \quad (3)$$

where the function $d(t, \mu_{\text{low}}(i), \mu_{\text{high}}(i))$ is defined as

$$d = \begin{cases} |t - \mu_{\text{low}}(i)|, & t \leq i \\ |t - \mu_{\text{high}}(i)|, & t > i \end{cases} \quad (4)$$

The distance between each gray level t from the mean value of its region is calculated by function $d(\cdot)$. Now, a cost function at each gray level i is determined to calculate an optimum threshold:

$$C_i = \sum_{t=0}^{I_{\text{max}}-1} [m_i(t)(1 - m_i(t))]^2 \quad (5)$$

According to above definition for the cost function, the gray level I_0 that provides minimum cost function is chosen as a threshold for binarization of the image I . The result of this step for one slice of a clinical CT scan data set is indicated in Fig. 3b. The original image of this slice which contains two non-isolated nodules (one small and one large) is shown in Fig. 3a.

This binarization process is well applicable for the majority of pixels inside the lung area. However, there are some bronchiole and nodule parts inside the lung area with intensities close to the lung wall intensities, which are mistakenly converted to the logical value of one, and are detected as non-lung parts. To solve this problem, in the second step, we applied two different sized windows. If the pixels located on two opposite sides of the window have similar logical values (e.g., zero), all pixels covered by this window will be converted to that logical value (e.g., zero). These two different sized windows help us to obtain a clean lung mask from small and large irrelevant (those nodules and bronchioles that are assigned, one as non-lung parts) parts in the lung area. The result of this step is given in Fig. 3c.

In the third step, non-isolated nodules connected to the chest wall are transferred to the isolated ones by applying two 45° rotated windows. If the pixels located on three sides of the

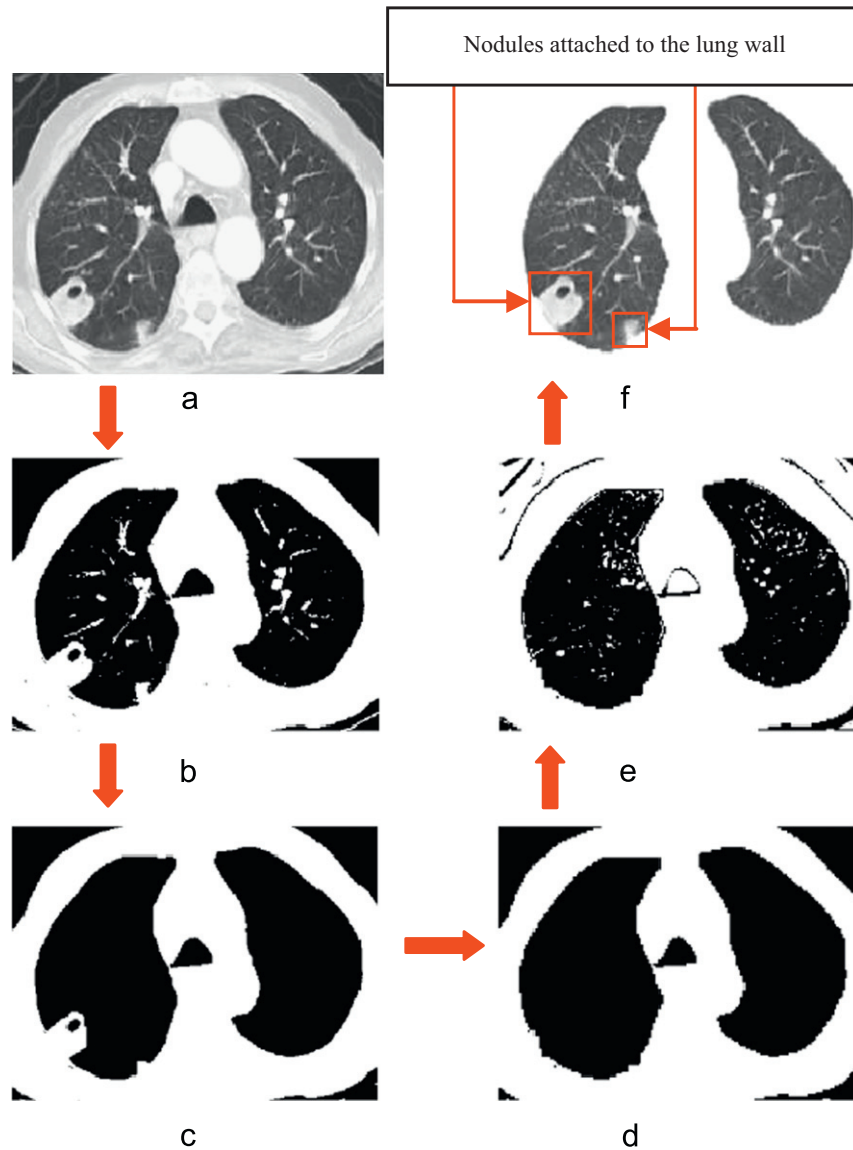


Fig. 3. All intermediate results of our lung segmentation algorithm. (a) original image; (b) result of the first step using the adaptive fuzzy thresholding proposed by Ye et al. [7]; (c) result of the second step of the lung segmentation algorithm; (d) result of the third step using 45° rotated square; (e) result of the fourth step of the lung segmentation algorithm; and (f) final segmented lung by active contour modeling.

window have logical value zero, all the pixels in this rotated square (which is shown in Fig. 2) will be converted to the logical value zero. Similar to above, two different sized windows are used for this step. This leads to the detection of small non-isolated nodules by the smaller window and large ones by the larger window. Contribution of this step in our lung segmentation method leads to detecting nodules with high detection rate. This is illustrated in Fig. 3d.

In the fourth step, two thresholds are applied on the values of the pixels in the original image to improve the result of the previous step. It is done by sweeping a 3×3 window on the original image. According to the gray levels of the corners and bony parts, appropriate thresholds are determined. By applying this step, corners (lower threshold) and bony parts (higher threshold) are made exclusive of lung parts. This achievement is shown in Fig. 3e, visually.

Finally, the result of the fourth step is applied as an initial mask (black parts) of the active contour model proposed by Lankton and Tannenbaum [13]. A global region-based energy that uses mean intensities is a well-known technique which was used

in this work. We call it *Yezzi energy code*, which was mainly proposed by Yezzi et al. [15]. Parameters of this ACM are maximum iteration (*Max-Iter*), localization radius (*Rad*) and weight of smoothing term (*Alpha*). Tuning these parameters is explained in Section 3. This ACM is useful to segment the borders of lung accurately and to exclude some tiny white parts existing in the lung areas of the result of previous step. The final result of our lung segmentation method, which is called *L*, is indicated in Fig. 3f. Transferring non-isolated nodules to the isolated ones is clearly presented in the result of this slice.

2.2. Nodule detection by SVM classifier

In this section, nodules are detected by classifying the segmented lung into two classes: nodule and non-nodule. In the following subsection, a method for the efficient extraction of features is described. Following this, the design of an SVM classifier using Gaussian RBF (radial basis function) kernel is described as the final subsection.

2.2.1. Extraction of 2D and 3D features

Feature extraction plays a significant role in any classification process. The efficient extraction of features yields better data discrimination. This also results in a better classification rate.

The most effective 2D stochastic feature for nodule detection is the pixel values. It is clinically observed that the gray level of nodules and some parts of the bronchioles are different from the background (lung areas). Therefore, as a feature, the mean values of the pixels in a defined neighborhood are calculated as:

$$M_{ij} = \frac{1}{9} \sum_{k,l=-1}^{+1} L(i+k, j+l) \quad (6)$$

where i and j are pixel coordinates, and L is the result of our lung segmentation method.

As mentioned before, segmental bronchus and some bronchioles have similar gray values compared with nodule gray values. Using two dimensional intensity-based features leads to similar label for windows with similar gray values. Regarding this issue, some bronchus areas are mistakenly labeled as nodule parts. To solve this problem, we apply this clinical fact that nodules have at least 5 mm length (the dimension of which is visible in an anterior view), but the length of bronchioles is often less than that of nodules. According to this fact, the succeeding and preceding slices of the slice under consideration (called the target slice) can be used to remove non-nodule parts.

Nodules usually repeat themselves in the preceding and/or succeeding slices at the same places. Regarding the clinical fact mentioned before, bronchioles do not exist in all neighbor slices. They might appear in some of them. Thus, by comparing the

target slice with neighbor slices, an anatomical 3D feature called *3D averaging*, is calculated as:

$$M_{ij}^p = \frac{1}{9} \sum_{k,l=-1}^{+1} L^p(i+k, j+l),$$

$$M_{ij}^+ = \frac{1}{q} \sum_{p=p+1}^{p+q} M_{ij}^p, M_{ij}^- = \frac{1}{q} \sum_{p=p-q}^{p-1} M_{ij}^p,$$

$$3D \text{ averaging} = M_{ij}^- M_{ij}^+ \quad (7)$$

where index p indicates the label of the slice, M_{ij}^p is the mean value of each window in the target slice, M_{ij}^+ is the average of mean values of the same coordinates in the succeeding slices, and M_{ij}^- is the average of mean values of the same coordinates in the preceding slices. For the first slice in each data set, M_{ij}^- is defined as M_{ij}^+ . And for the final slice, M_{ij}^+ is defined as M_{ij}^- . The parameter q is the number of considered slices, which depends on data set slice thickness. It is defined as

$$q = \frac{c}{T}, \quad T: \text{thickness of slices} \quad (8)$$

As mentioned above, the minimum length (anterior view) of nodules is usually 5 mm. Thus, c is generally equivalent to 5.

When the mean value of a window in the target slice is high, it might be labeled as a nodule in the testing process. But if the mean values of the windows in the same places of preceding and/or succeeding slices (M_{ij}^-, M_{ij}^+) are low, the value of *3D Averaging* will be low, too. Thus, this window might be labeled as non-nodule (bronchus). Low values for M_{ij}^- and M_{ij}^+ lead to

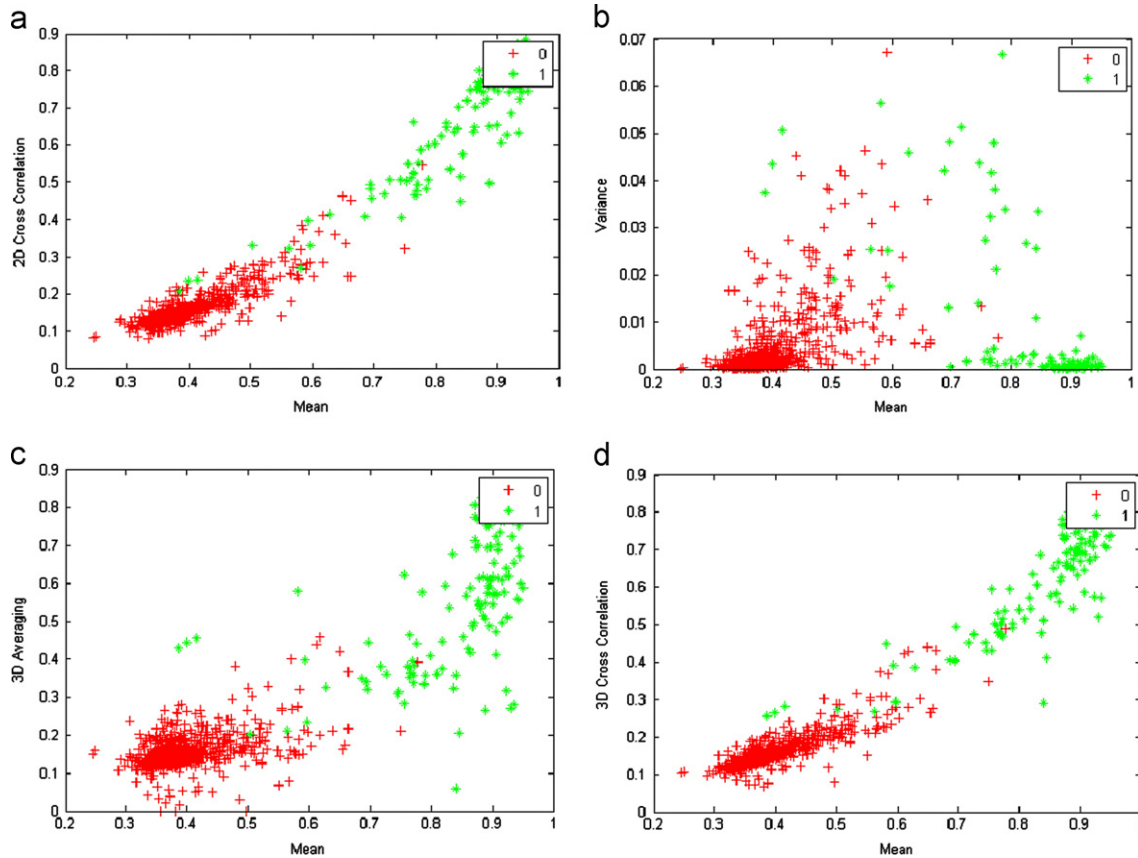


Fig. 4. Comparison of 5 features calculated for 1000 windows. X-axis in all images is mean values of gray levels in each window. Y-axis in (a) is the cross correlation between each window and its neighbor windows in the target slice. Y-axis in (b) is the variance of each window. Y-axis in (c) is *3D Averaging* calculated in Eq. (7). Y-axis in (d) is the cross correlation between each window and the window located in the same place in previous and next slices. Red plus and green asterisk signs are non-nodule and nodule parts (in the lung area) respectively. (For interpretation of the references to color in this figure legend, the reader is referred to the web version of this article.)

correct labeling of non-repeating bronchus as non-nodule parts in the testing process.

These efficient 3D features lead to the accurate detection of nodule, and a decrease in the number of FP.

In Fig. 4, five features are calculated for 1000 windows of the lung area which include two nodules. Nodule parts are labeled as one (green asterisk) and non-nodule areas are labeled as zero (red plus sign). In all plots, mean values are considered as the X axis and another feature is considered as the Y axis. Efficiency of *Mean* is obviously indicated in all four plots. As indicated in Fig. 4c, d, the *3D Averaging* and *3D Cross Correlation* are more discriminative. The values of these features for nodule labels are much more than those of non-nodule labels. These plots verify our claims about these two different kinds (Mean and 3D) of features for CT lung images.

2.2.2. SVM classification

We utilize SVMs in the binary classification setting. The original SVM algorithm was invented by Vapnik [16]. SVM finds the maximum-margin hyper-plane that divides the data points. Let $\{x_1, x_2, \dots, x_n\}$ be training data points with d -dimensions and corresponding labels $\{y_1, y_2, \dots, y_n\}$ where $y_i \in \{-1, 1\}$. In the simplest form, SVMs are hyper-planes that separate the training data by a maximal margin. The training instances that lie closest to the hyper-plane are called support vectors. All vectors lying on one side of the hyper-plane are labeled as -1 , and all vectors lying on the other side are labeled as $+1$. Non-nodule areas, which are assigned zero labels in the previous sub-section, are converted to -1 for appropriate implementation in this sub-section.

To construct an optimal hyper-plane, SVM uses an iterative training algorithm (the QuadProg method) which is used to minimize an error function. In the simplest case, the error function is defined as

$$\frac{1}{2} w^t w + C \sum_{i=1}^N \zeta_i \quad (9)$$

subject to the constraints:

$$y_i (w^t \varphi(x_i) + b) \geq 1 - \zeta_i, \quad \zeta_i \geq 1, \quad i = 1, \dots, N \quad (10)$$

where C is the capacity constant, w is the vector of coefficients, b is a constant and ζ_i are parameters for handling non-separable data (inputs).

In this paper, the Gaussian RBF is applied as a kernel. Because of its non-linearity, this kernel is suitable for some non-separable data [17,18]. Applying RBF helps us to reduce the number of required slices of a data set for the training process.

The result of this section is an image with gray level values of zero for non-nodule areas (all -1 labels are converted to zero to have a gray scale image) and one for nodule pixels. This result contains a detected nodule (and some tiny bronchioles as FPs) with coarse borders. In the next section, we propose a method to improve nodule borders and the number of FP.

2.3. Active contour-based nodule contour extraction

In the previous section, using 3×3 windows for labeling nodules and non-nodules results in some small deformation in the contours of detected nodules. Active contour modeling is applied to resolve this problem. In the process of active contour, tiny parts, which were mistakenly detected as nodules, are omitted, in turn reducing the number of FP.

In this paper, the application of active contour modeling in lung nodule segmentation is proposed. We proposed the primary idea and results in [14]. In this section, the active contour model proposed in [13] is used. This is known as a robust and effective active contour modeling of thin edges, such as the border between nodule and lung. This algorithm was tested on different kinds of images, including medical and non-medical ones. The results indicate high performance as well as robustness of this method on the noisy images [13,15]. The active contour, using the result of previous section as the initial contour, is applied on the original image (I). If some small parts are not detected by the lung segmentation algorithm, they will be segmented using I as an input of the active contour model. Results are shown in Fig. 5. For better visualization, final segmented nodules (called *Nod*) are shown alongside the lung segmented results.

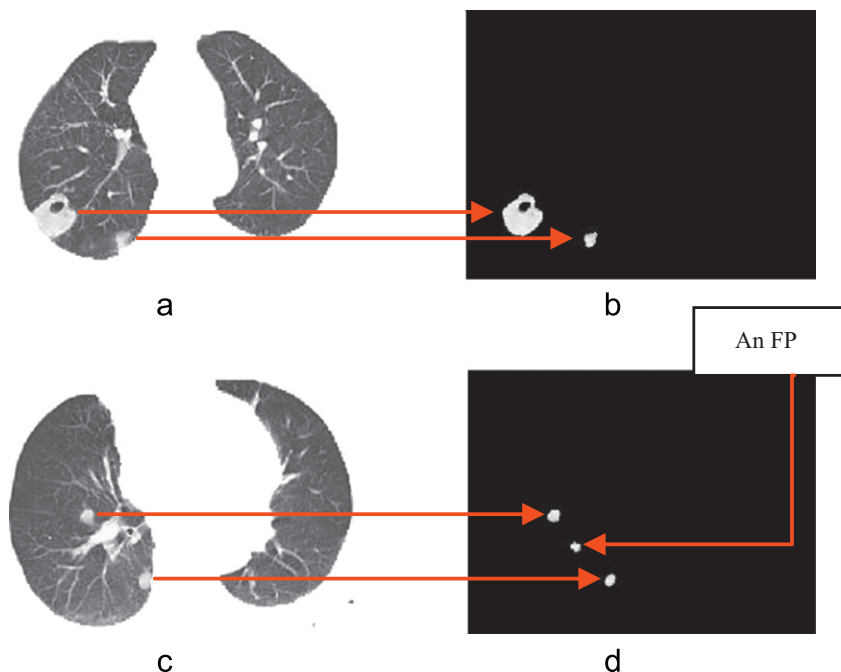


Fig. 5. Final segmented nodules and their segmented lungs: (a) result of lung segmentation; (b) final segmented nodule of image (a); (c) result of lung segmentation for another slice; and (d) final segmented nodule of image (c). An FP is shown in (d).

2.4. Nodule connectivity recognition

The location of a nodule can be determined by the lung tissue which is attached to the nodule. The original image is classified into four classes: lung wall (LW), parenchyma (PA), bronchioles (BR) and nodules (ND). If these four classes are segmented accurately, nodule will be recognized as its connected tissue. If class ND is connected to class LW or to BR, that class will be a lung wall attached nodule or a bronchiole attached nodule, respectively. Also, if class ND is completely covered by class PA, that class is called solitary nodule. In this section, initially the original

image is portioned into four classes by applying results of previous sections. Then, a nodule is examined to see whether it is connected to LW, BR or not (solitary) by considering the neighbor pixels of nodules.

The result of the previous section (recall: *Nod*) can be used as class ND in a slice. Due to some probable errors in nodule segmentation, we apply a dilation process on the image *Nod* using a suitable structuring element:

$$ND = \text{dilate}(Nod) \quad (11)$$

The result of our lung segmentation algorithm, which is called *L*, can be applied to detect class LW. All pixels that are not detected as the lung area in Section 2.1 are considered as the class LW:

$$LW = \bar{L} \quad (12)$$

All pixels detected in image *L* and not detected in image *Nod* are considered as PA and BR classes:

$$PA \cup BR = L \cap \overline{Nod} \quad (13)$$

To discriminate these two classes from each other, we use a simple thresholding. By considering the histogram of a sub-image containing only PA and BR classes (Fig. 6), the initial threshold is obtained. Then, the appropriate threshold is determined empirically.

For nodule connectivity recognition, all gray values of neighbor pixels of the nodule have to be considered. To simplify this process, we assign specific labels to these classes. In Fig. 7, the result of the labeled image is shown.

By sweeping windows (through the labeled image), which are located in the borders of class ND, pixels in the neighborhood of the nodules are detected. Mean values of those neighbor pixels are calculated for each window. For example, for a solitary nodule, all these mean values are labeled with a value of PA, and also, for a lung wall attached nodule, these mean values are PA label values for some windows and LW label values for some others (such nodules are shown in Fig. 7). Therefore, by averaging label values of neighbor pixels, tissues attached to the nodule are recognized and consequently, the location of the nodule is determined as its attached tissue. In Figs. 7 and 8, the final result of this stage is shown for two nodules attached to the lung wall and one nodule attached to the bronchiole, respectively.

3. Experimental results

In this section, results of the proposed method are presented and the values of some parameters are determined. In the experimental results, four groups of data sets are used.

In the first group, four clinical data sets with 13 nodules approved by medical experts are used. There are 45 slices/scans

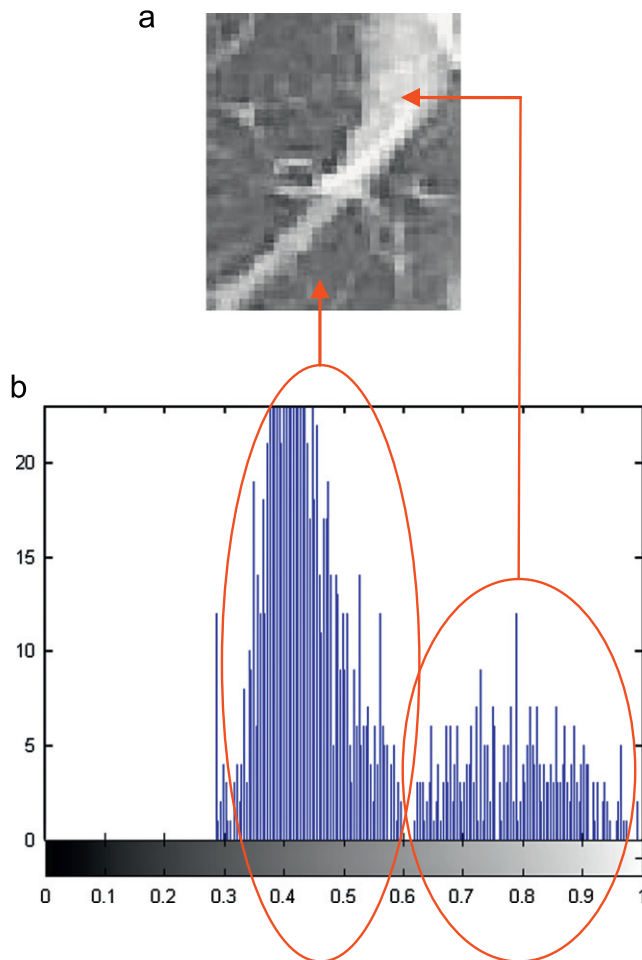


Fig. 6. (a) A sub-image containing PA and BR classes and (b) histogram of the sub-image. The ranges of PA and BR classes are approximately shown by the bigger and smaller ellipsoids, respectively.

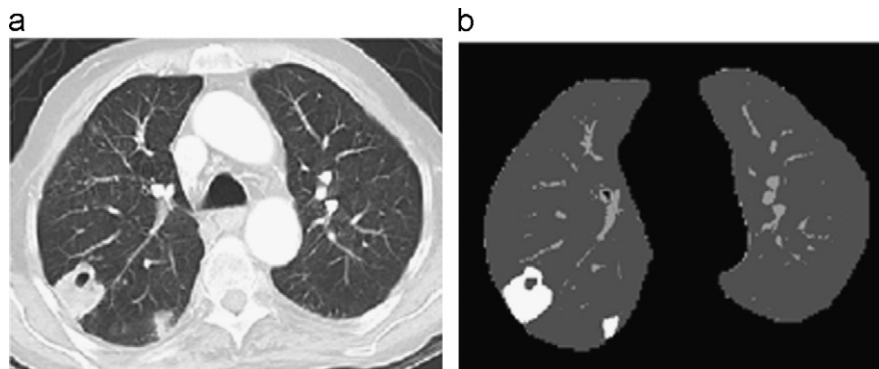


Fig. 7. Final result of labeled image into 4 classes beside their original image (two nodules attached to the lung wall): (a) original image and (b) labeled image.

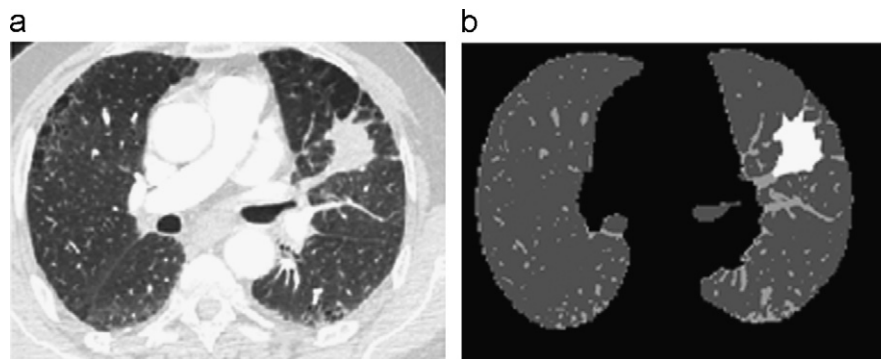


Fig. 8. Final result of labeled image: (a) original image and (b) result of labeling lung tissues (four labels: LW, PA, BR and ND). One bronchiole attached nodule exists.

Table 1

Characteristics of our data sets categorized in four groups. Each nodule is assigned to a location and shape type.

Data	Number of scans per group	Thickness (mm)	Number of nodules per type						
			Different locations			Different shapes			
			Solitary	BR attached	LW attached	Solid	Non-solid	Cavitary	Total
Clinical-1	4	5	5	1	7	11	2	0	13
Clinical-2	4	0.625	1	1	4	4	0	2	6
ANODE09	5	1	12	16	11	–	–	–	39
LIDC	50	1.25	124	118	155	–	–	–	397

among which 4 data sets are of 5 mm thickness. Also, there are 11 solid and 2 non-solid nodules in these data sets. Here, we have 7 lung wall attached, 1 bronchiole attached and 5 solitary nodules.

In the second group, there are 4 data sets including about 450 slices/scans with 0.625 mm thickness. There are 4 solid and 2 cavitary nodules in these images. Four of these nodules are lung wall attached, 1 of them is bronchiole attached and the other one is solitary. Table 1 identifies characteristics of our data sets. Clinical -1 and -2 data sets were obtained in TABA medical imaging center at Shiraz University of Medical Sciences. The radiologist of this center, who has practiced for at least 20 years, helped us to get hand-drawn contours of nodules.

The third group, introduced by Ginneken et al. [19], was provided from ANODE09. This group contains 5 data sets including 39 nodules. The annotations of these 39 nodules are available on ANODE09 web site. According to the information of nodules mentioned in [19], around 31% of nodules are solitary, 41% are bronchiole attached, and 28% are lung wall attached. Also, 45% of nodules are large nodules (the diameter of a large nodule is considered to be equal to or bigger than 5 mm).

The fourth group is from ELCAP (Early Lung Cancer Action Program) which is one of LIDC groups. The data and annotations are freely available in [20]. This group contains 50 patients and 397 nodules were provided by four radiologists. These 4 observers indicated nodules in a two step process, first blinded, next unblinded, so that they could see the results of the other 3 readers. True positive nodules were indicated by at least 2 of 4 radiologists. As official reports [20], 31% of nodules are solitary, 30% are bronchiole attached and 39% are lung wall attached. The mean diameter of nodules is 8.5 mm with standard deviation of 3.6. It means that less than 5% of nodules are small (the diameter of a small nodule is considered to be less than 5 mm).

The proposed method was applied on the above mentioned data sets (Table 1). First, lungs were segmented by the proposed method which was described in Section 2.1. In the first step of lung segmentation algorithm, all slices were converted to binary images by fuzzy adaptive thresholding. Then, we applied two

windows with 5×5 and 23×23 sizes to obtain a hole-free lung mask. These windows help us to remove small (by 5×5 windows) and large (by 23×23 windows) irrelevant parts (bronchiole and nodule areas which were labeled as a part out of the lung) in the lung area. These sizes were chosen based on the sizes of irrelevant parts. In the third step, 25×25 and 50×50 rotated windows were utilized to transfer small and large non-isolated nodules (lung wall attached nodules) into isolated ones. The sizes of rotated windows were chosen for detecting different sized nodules. In the fourth step, two thresholds were applied by sweeping a 3×3 window to exclude corners (lower threshold) and bony parts (higher threshold). Each of the nine pixels having the average of intensities lower than 0.32, and more than or equal to 0.99, is converted to the logical value one in the result of the previous step. Result of this step was applied as the initial contour of the active contour model to extract the border of the lung area delicately. Parameters of ACM were assigned as: $Max-Iter = 120$, $Rad = 8$, $Alpha = 0.2$. Regarding the similarity between initial mask and lung contours, 120 iterations are adequate for the parameter $Max-Iter$. Also, the value of Rad , which is a tradeoff between more global and more local contour extraction, was chosen 8 pixels. The last parameter $Alpha$ was determined as 0.2 to obtain smoother result. The results of different steps of our lung segmentation algorithm using mentioned windows and ACM parameters are illustrated in Fig. 3. The proposed lung segmentation algorithm leads to fine segmentation of lung area and accurate transfer of all non-isolated nodules to the isolated ones.

Segmented lungs were divided into 3×3 windows in which all nine pixels were located in the lung mask. Window size selection is a compromise between higher resolution (in the classification process) and faster algorithm. Smaller windows (i.e. 1×1 or 2×2) have the problem of more time complexity for training and increasing the number of FP. Larger windows (i.e. 5×5 or larger) cause lower resolution of reconstructed image after classification and miss some tiny nodules. Thus, for better resolution and faster algorithm, simultaneously, we used a 3×3 window. In the training process, these windows were labeled as

nodule (+1) and non-nodule (−1). The training process was done by the QuadProg method with 1500 maximum iterations. In this process, 15 scans were selected from all four groups (24% of all data sets were used in the training process). Then 2D and 3D efficient features are calculated for them. Pixel gray value is the most effective 2D feature. Because pixel values of the lung area mostly belong to [0.35,0.65] (black=0; white=1), and in the nodule area, pixel values mostly belong to [0.7,0.95]. Using 2D features leads to the detection of some bronchioles as nodule parts mistakenly. That is why we proposed 3D *Averaging* and 3D *Cross Correlation* features. During test, label of each window (for all three groups of data sets) was determined by SVM classifiers based on their feature values. Result of the classification was used as the initial contour of the active contour model. In this step, *Max-Iter* of ACM was assigned 40, because contours of detected nodules resulted from SVM classifier are very close to real contours of nodules. As illustrated in Fig. 5, application of ACM leads to delicate extraction of detected nodule borders.

Finally, lung tissues are labeled by four specific labels, as:

$$LW = 0, \quad PA = 0.3, \quad BR = 0.6, \quad ND = 1 \quad (14)$$

Pixels in neighborhood of segmented nodules are detected by sweeping 5×5 windows through the labeled image. In this stage,

those windows, which contain 5–21 (are obtained empirically) pixels inside the class ND and the rest of them (4–20 pixels) outside the nodule, are considered as the nodule neighboring windows. Mean label values of neighboring pixels are calculated for each window. These mean values are 0.3 for solitary nodules, between 0 and 0.3 for lung wall attached nodules and between 0.3 and 0.6 for bronchiole attached nodules. Results of tissue labeling are indicated in Figs. 7 and 8.

In Fig. 5, results of our method for two different slices are indicated. There are one large cavitory non-isolated nodule and one small non-isolated nodule in the image (a). In the result (b), both nodules are accurately segmented with no FP. Transferring non-isolated nodule into isolated one was done by proposing the third step of our lung segmentation algorithm. In the image (c), there are one small isolated nodule and one non-isolated nodule. In the result (d), both of them are segmented with one FP. There are some results of the proposed method in the other slices (different parts of the lung for different patients) in Fig. 9. In these results, there is no FP with fine nodule segmentation using active contour modeling. Cavitory nodules are segmented in Fig. 9b. One of these nodules is attached to the chest wall and a bronchiole. It transfers to the isolated nodule very well. Experimental results in Fig. 9f reveal that jagged nodule is segmented accurately. Using ACM leads to the segmentation of nodules with different shapes.

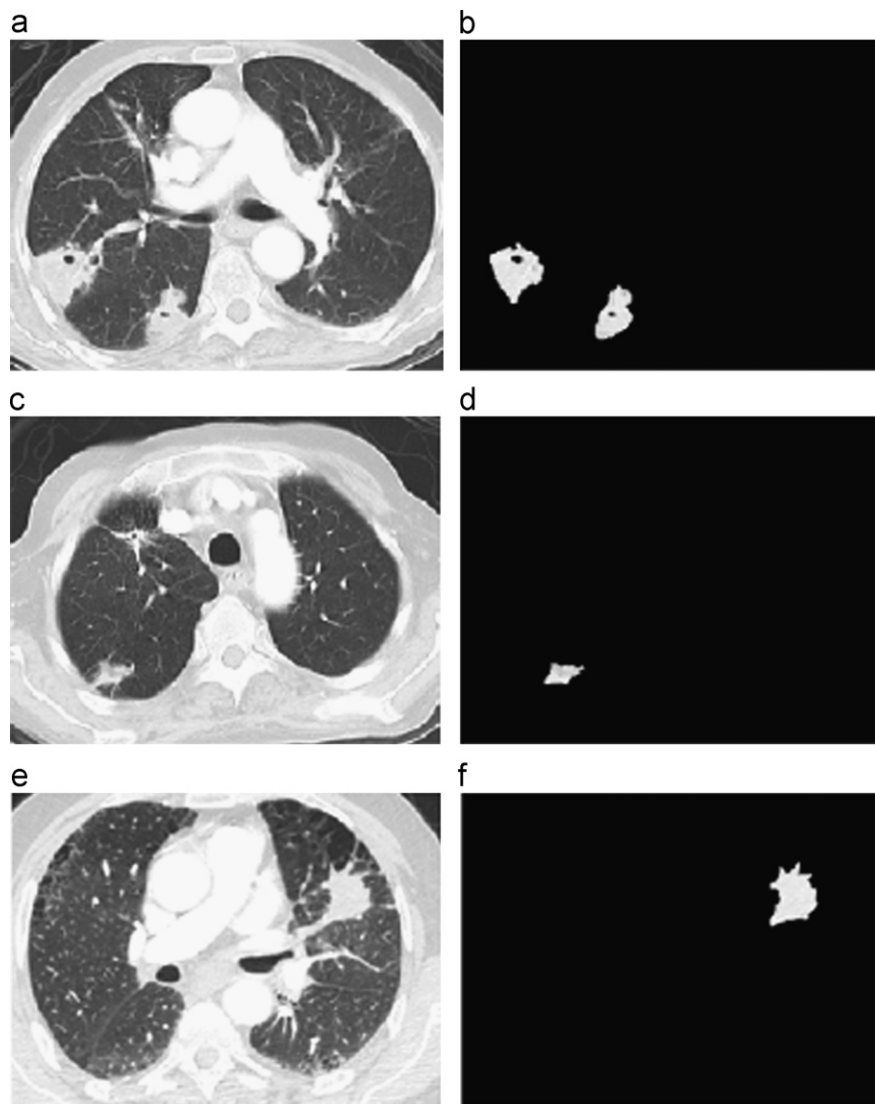


Fig. 9. Results of the proposed method; (a), (c) and (e): original images; (b), (d) and (f): final results for input images (a), (c) and (e) respectively.

In this paper, an accurate criterion is defined to determine the accuracy of detection and localization of the nodules segmentation algorithms. Assigned labels in the test process for each 3×3 window are compared with correct labels determined by TABA radiologist. This criterion, which is named *Segmentation Accuracy* (S.A.), is defined as

$$S.A. = \frac{1}{w} \left(w - \sum_{i=1}^w |Assigned\ label - Correct\ label|_i \right) \quad (15)$$

where w is the total number of windows located in the lung area and i is the considered window. All the labels are one (nodule windows) or zero (non-nodule windows). Thus, the value under summation in Eq. (15) is zero for correct detections and one for incorrect detections. If the difference between assigned label and correct label is zero, S.A. will be increased and if it is nonzero, S.A. will be decreased. For example, if the total number of windows is $w=3000$ (in the lung area of one slice) and incorrect assigned labels are 50 windows (result of summation), S.A. will be 0.983. In this example, detection rate is 100%, but S.A. is 0.983. Because of some miss-classification, detected nodules are not segmented completely. Therefore, this value indicates the accuracy of our segmentation method. That is why S.A. is more accurate than the detection rate.

Table 2 indicates the S.A. for different kernel functions of SVM classifier calculated for those slices which contain at least one nodule. The first column of S.A. (S.A.1) is calculated for the case that both of the nodules are detected (two slices of this CT scan are shown in Figs. 5 and 9a and only a few windows are incorrectly labeled (detection rate=100%). The S.A.1 indicates the effect of using different kernel functions on the segmentation of nodules in one CT scan. The second column of S.A. (S.A.2) is calculated for all data sets of Clinical-1 and -2 where 90% of the nodules are detected. The values of this column are about 1.5% lower than the first ones, because, two nodules are completely missed in the second column. On the other hand, because of some other miss-segmentation of the pixels around or inside the other nodules (that are distributed in eight CT scans), there is about 1% reduction in going from S.A.2:RBF to S.A.2:MLP (multi-layer perceptron). Thus, the influence of different kernel functions using several CT scans is clearer than this influence using one CT scan. Results of different kernel functions illustrate that the RBF performs better than the others.

The third column of Table 2 indicates the Dice Coefficient of the nodule segmentation algorithm using different kernel functions. This criterion is defined as:

$$Dice = \frac{2 \times TP}{(TP+FP)+(TP+FN)} \quad (16)$$

where TP (true positive) is the number of windows (each window contains nine pixels) that are correctly labeled nodule. The FP is the number of windows that are mistakenly labeled nodule. And, the FN (false negative) is the number of windows that are

mistakenly labeled non-nodule. The Dice Coefficient, the same as the S.A. criterion, indicates that the RBF is the best kernel function.

In Fig. 13, results of our labeling stage (for nodule connectivity recognition) are illustrated. In the first result (b), there are 2 very small lung wall attached nodules and 2 tiny FPs. These two FPs are recognized as bronchiole attached nodules. If they were nodules, this recognition would be correct. In the second result (d), 2 nodules are recognized as bronchiole attached nodules. On the whole, having assumed that nodule segmentation is done accurately, there is no considerable error in our nodule connectivity recognition algorithm.

4. Discussion

In this section, we discuss about the results of the proposed method and compare them with the results of other high performance algorithms.

There are two very important steps in our nodule detection and segmentation algorithm. The first one is proposing 3D features in nodule detection method to remove bronchioles. When only the 2D features are considered, such bronchioles are mistakenly detected as nodules. In Fig. 10, the effect of applying 3D features is indicated. Images in column (a) show the original images. Images in column (b) illustrate results of our nodule detection method without using 3D features, and finally, the images in column (d) are final results of our nodule detection method. Comparing column (b) and (d) indicates that some bronchioles are mistakenly detected as nodules in column (b), and there are no FPs in results of column (d) except one FP in row (6).

The second important step is applying ACM to segment nodules finely. As described previously, the detected nodules are applied as an initial contour of ACM. Due to this initialization, ACM fits true positions (nodule borders) by a few iterations. This step leads to accurate extraction of nodule borders and removes tiny non-nodule parts which are indicated in column (c) of Fig. 10. Images in this column are results of our nodule detection method using 2D and 3D features without using ACM. The effect of applying ACM on our nodule segmentation algorithm is clearly illustrated when comparing images in column (c) and (d). Accurate nodule segmentation results are shown visually in rows (2), (3), and (4).

Shimoyama et al. [12] proposed a new lung segmentation algorithm using active contour modeling with the main contribution of detecting non-isolated nodules. They used a contour of each slice for the succeeding slice as an initial mask (as described in Section 1). Because of their good performance in detecting large non-isolated nodules, we compare our method with this method. However, their method depends on the thickness of slices. The comparison of their method and our lung segmentation algorithm is indicated in Fig. 11. In this figure, we used the first data set (5 mm thickness). Because of the high thickness of slices, the proposed method in [12] failed in segmenting a small part near the small nodule. Also, the airway and some mid parts are mistakenly segmented to the lung areas, which are segmented by our method correctly.

Ye et al. [7] proposed a method for nodule detection. Their algorithm is very effective to detect very small nodules and reduce the number of FP, and hence we compare our algorithm with their method. In their lung segmentation algorithm, they considered small non-isolated nodules, but not for large ones. Figs. 12 and 13 show that the performance of our proposed algorithm is better than Ye's algorithm in this situation. Our method can detect large nodules using rotated windows with different sizes, where Ye's algorithm lacks this capability. On the

Table 2
Segmentation accuracy and dice coefficient of proposed method using different Kernel functions of SVM classifier

Kernel function of SVM	Segmentation accuracy ^a	Segmentation accuracy ^b	Dice coefficient (%)
Gaussian RBF	0.995	0.981	82
Linear	0.989	0.970	71
Polynomial-order 3	0.995	0.978	77
MLP-scale1	0.991	0.972	74

^a For the case that all nodules are detected.

^b And dice: for all of our clinical data sets that 90% of the nodules are detected.

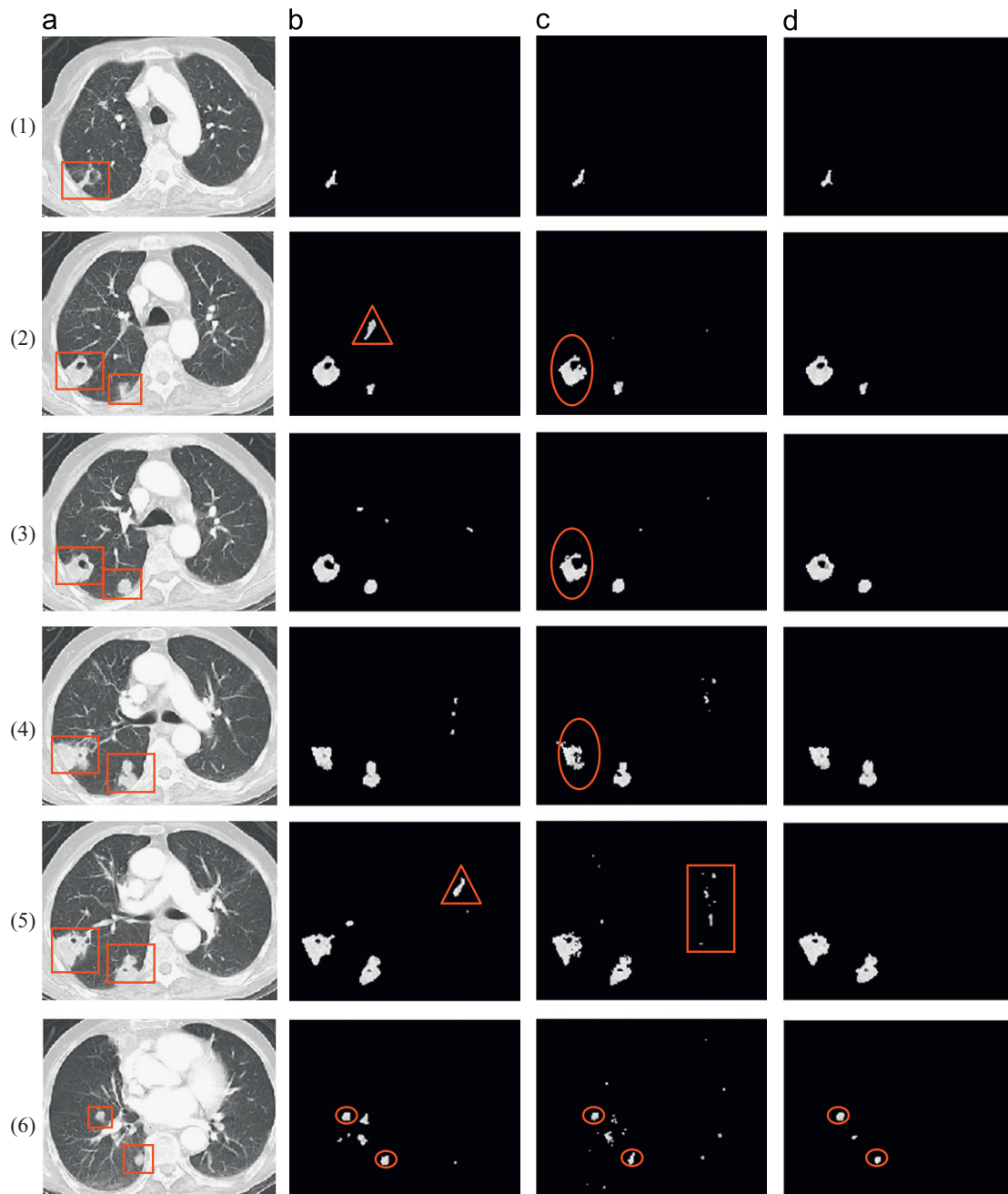


Fig. 10. Representing the effect of two important steps of our nodule detection algorithm. Images in column (a) are original images in different slices of a patient. Images in column (b) are results of our nodule detection method without using 3D features (using 2D features and ACM). Images in column (c) are results of our nodule detection method with use of all features without using ACM. Images in column (d) are final results of our nodule detection method using all 2D and 3D features and also using ACM. In column (a), nodules were signed by red squares. Red triangles in (2b) and (5b) images show that the bronchioles were detected as nodules mistakenly (without using 3D features). The effect of using ACM to segment nodules finely was shown by red ellipsoids in (2c), (3c) and (4c) images compared with the same rows in column (d). The red quadrangle in (5c) image shows irrelevant small parts that are removed in (5d). Red circles in final row indicate detected nodules. (For interpretation of the references to color in this figure legend, the reader is referred to the web version of this article.)

other hand, our method fails in detecting tiny nodules with complicated anatomical locations.

Table 3 shows a comparison of our nodule detection and segmentation algorithm with two well-known methods for eight clinical data sets (Clinical-1 and -2) including 19 nodules. There are two non-solid nodules which were not detected by our method. There are five large non-isolated nodules which were not detected by Ye's algorithm. In Table 3, the comparison is also done by detection rate. This value is calculated by dividing the number of detected nodules to the total number of nodules in a data set. In Table 3, the accuracies of nodule segmentation

algorithms are compared by our proposed criterion (S.A.) and the Dice Coefficient. Because of the weakness of Ye's algorithm in detecting large non-isolated nodules, these values of Ye's algorithm are less than that of the proposed method.

Okada et al. [21] proposed an algorithm for 3D tumor segmentation. By using shape-index to detect nodules, they were successful in segmenting spherical nodules, but their method fails in segmenting non-spherical nodules. We have used our lung segmentation algorithm as the pre-process of Okada's algorithm. It means that we applied Okada's algorithm instead of our nodule detection and nodule contour extraction algorithm. This is

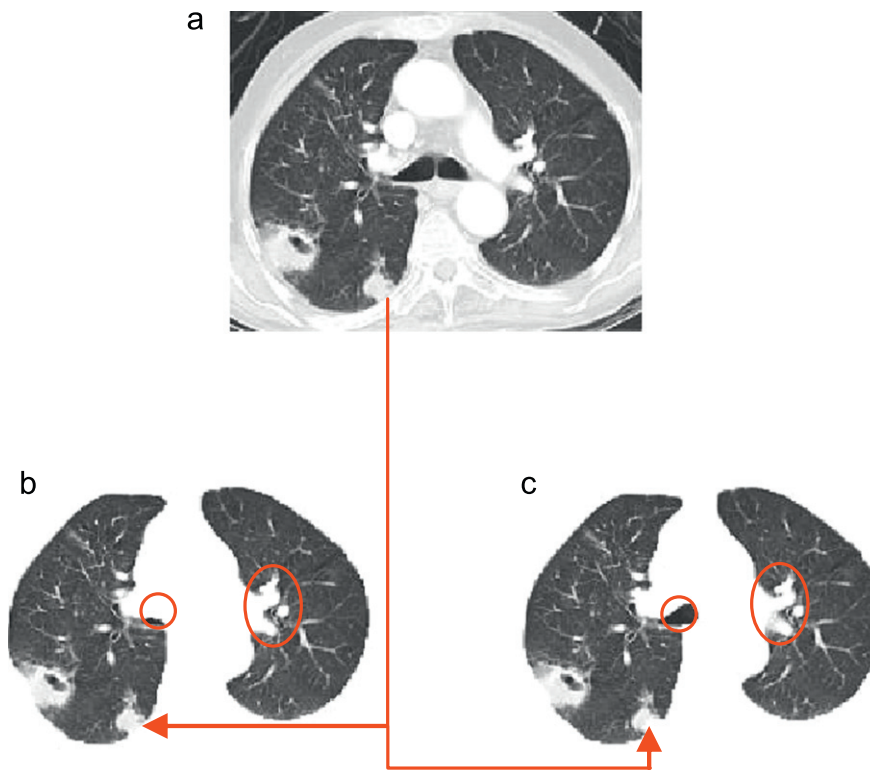


Fig. 11. Comparison of our lung segmentation method with proposed method in [12]. (a) Original image; (b) segmented lung by our method; and (c) segmented lung by [12]. Ellipsoid parts indicate some non-lung areas which are segmented out of lung only by our method. The airway is segmented out of the lung by only our method (circle areas). A part of small nodule is not detected by [12]. It is detected in our method (red flashes). (For interpretation of the references to color in this figure legend, the reader is referred to the web version of this article.)

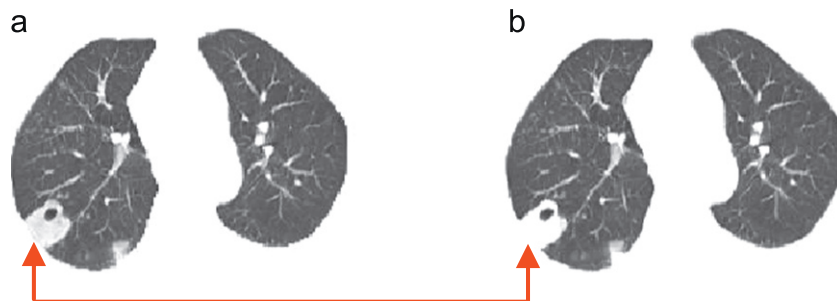


Fig. 12. Comparison of our lung segmentation method with proposed method in [7]. (a) Segmented lung by our method; and (b) segmented lung by Ye's algorithm [7]. Failed segmentation for large non-isolated nodule is shown by the red flashes (the nodule was detected as the lung wall by proposed method in [7]). (For interpretation of the references to color in this figure legend, the reader is referred to the web version of this article.)

our-Okada in Table 3. This combination leads to the detection of all nodules but one. However, Okada's algorithm is unable to segment nodules with irregular shapes accurately. Although the detection rate of our-Okada is higher than that of our method, the dice coefficient of our-Okada's method is 4% less than that of our method. The first reason is that the FP number of our-Okada's method is more than that of our method. The second reason is the weakness of Okada's method in extracting the contours of irregular shaped nodules. These types of nodules are detected by Okada's method, but their contours are not accurately extracted.

For better comparison between the proposed method and other methods, public data sets were used. Table 4 indicates the detection rates of different methods using the ANODE09 database. The best detection rate belongs to ISICAD (E), and the second best detection rate belongs to our method. Detection rates of other methods are lower than of these two methods. In system E, region

growing was used to segment lung areas. To detect nodules, the shape index and curvedness were computed at a fixed scale of one voxel. Also, k -nearest neighbor classification (KNN) was used to remove False-positive candidates. Because of the clinical fact mentioned in Section 2.2.1, the detection rate of system E is higher than that of our method. In order to remove all nodules smaller than 5 mm, we compared the axial dimension of bronchioles and nodules, and removed all candidates with the length less than 5 mm. As mentioned, in ANODE09 data sets, 55% of nodules are smaller than 5 mm and the rest of them are detected by our method. If parameter c in Eq. (8) is decreased from 5 to 4 or 3, the detection rate, as well as FP/Scans, will increase. As indicated in Table 4, the detection rate of our method for FP number of 8 is 66.2%. This rate is more than 45%, because parameter c is reduced to 3.

In Table 5, the detection rates of some other methods are compared using LIDC database. Bearing in mind the size of

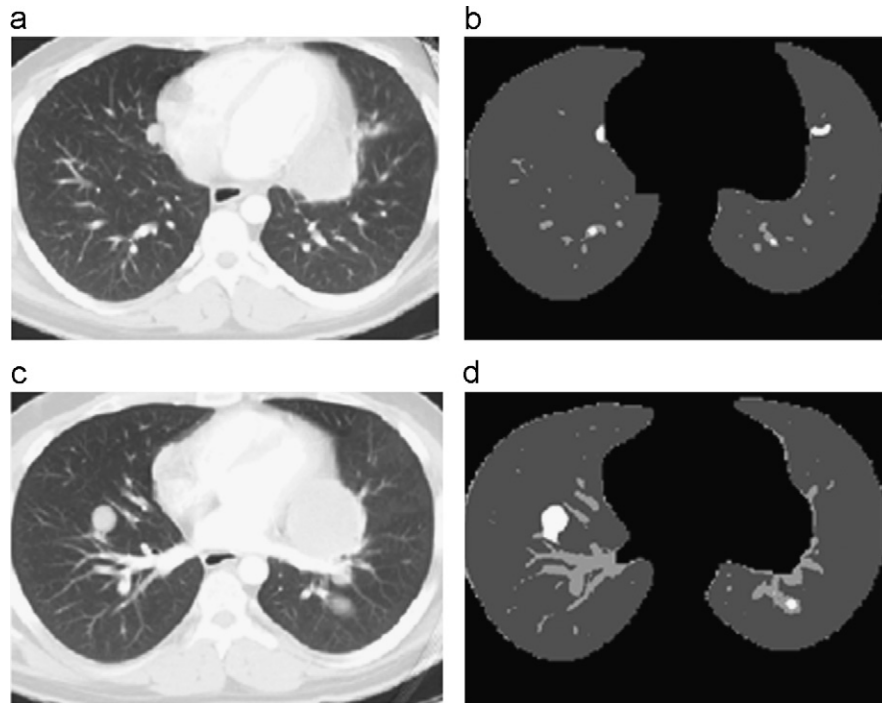


Fig. 13. Results of our method for tissue segmentation: (a) original image; (b) the result of image (a) with two LW attached nodules and tiny FPs; (c) the original image; and (d) the result of image (c) with two BR attached nodules with no FP.

Table 3

Comparison of our method with two well-known algorithms for 19 nodules.

Methods	Ye et al.[7]	Our-Okada [21]	Our method
Detected nodules	14	18	17
FP/scan	4.50	6.38	5.63
Detection rate (%)	74	95	90
Dice coefficient (%)	76	78	82
Segmentation accuracy (S.A.)	0.976	0.976	0.981

Table 4

Detection rates of different methods using ANODE09 datasets.

FP/scans	1/8	1/4	1/2	1	2	4	8	Average (%)
A. FujitaLab [19]	13.5	15.0	19.3	23.7	24.6	26.1	26.1	21.2
B. RG-Magic [22]	11.1	15.0	18.8	26.6	37.7	45.4	48.8	29.1
C. Magic-Ants [23]	4.3	5.8	14.0	23.2	33.3	45.4	51.7	25.4
D. Pisa team [24]	6.8	12.6	20.8	28.5	35.7	46.4	54.6	29.3
E. ISICAD [25]	45.0	48.8	57.0	63.8	71.2	76.8	79.7	63.2
F. Philips [26]	3.4	6.7	12.7	20.8	27.6	39.2	51.2	23.1
Our method	15.3	19.1	26.5	34.8	45.0	57.7	66.2	37.8%

Table 5

Detection rates of some other methods comparing with our method.

Methods	Detection rate (%)	FP/scan
Dehmshki et al. [27]	90	14.6
Taghavi et al. [11]	88	10.3
Farag et al. [28]	79	Not declared
Our method	89	7.3

nodules in these 50 data sets, the detection rate of our method is relatively high. As mentioned at the beginning of this section, around 5% of nodule diameters are less than 5 mm. Thus, most nodules were detected by our method with a reasonable FP number.

5. Conclusion and future work

In this paper, we proposed an automatic lung nodule detection, segmentation and recognition algorithm. Our algorithm needs only one input, which is the thickness of slices used for the calculation of 3D features, to start the procedure.

In our lung segmentation algorithm, an efficient combination of two classic methods leads to the segmentation of lung areas with segmenting large and small non-isolated nodules as the parts inside the lung area. The 45° rotated window plays a critical role in this process. In our nodule detection method, 2D stochastic and 3D anatomical features are applied in an SVM classifier. In this stage, nodules are detected with a high detection rate. Proposing 3D anatomical features leads to remove bronchioles which are mistakenly detected as nodules when only 2D features are considered. Furthermore, detected nodules are used as the initial contour of active contour modeling for a delicate extraction of nodule borders and so, high magnitudes of S.A. and the dice coefficient were achieved. Active contour modeling contributes two important achievements: firstly, all nodules, especially cavities, are segmented accurately, and secondly, some tiny bronchioles remaining in the detection step are removed, leading to a reduced FP number. In the last step of our algorithm, lung tissues (lung wall, parenchyma, bronchiole and nodule) are segmented and labeled to recognize the connectivity of segmented nodules.

Looking forward, we propose an updated algorithm comprised of a 3D reconstruction of the nodules which can further be used to calculate the volume of the nodules.

References

- [1] Y. Zheng, K. Steiner, T. Bauer, J. Yu, D. Shen, C. Kambhamettu, Lung nodule growth analysis from 3D CT data with a coupled segmentation and registration framework, in: Proceedings of the IEEE Computer Vision Conference, 2007, pp. 1–8.
- [2] American Cancer Society. (2009). Cancer fact and figures [Online]. Available: <http://www.cancer.org>.

- [3] D. Wu, L. Lu, J. Bi, Y. Shinagawa, K. Boyer, A. Krishnan, M. Salganicoff, Stratified learning of local anatomical context for lung nodules in CT images, in: Proceedings of the 2010 IEEE CVPR Conference, pp. 2791–2798.
- [4] C. Lei, L. Xiaojian, Z. Jie, C. Wufan, Automated lung segmentation algorithm for CAD system of thoracic CT, *J. Elsevier Med. Coll. PLA* 23 (2008) 215–222.
- [5] M. Silveira, J. Marques, Automatic segmentation of the lungs using multiple active contours and outlier model, in: Proceedings of the 2006 IEEE EMBS, pp. 3122–3125.
- [6] J.M. Kuhnigh, V. Dicken, L. Bornemann, A. Bakai, D. Wormanns, S. Krass, H.O. Peitgen, Morphological segmentation and partial volume analysis for volumetry of solid pulmonary lesions in thoracic CT scans, *IEEE Trans. Med. Imaging* 25 (2006) 417–434.
- [7] X. Ye, X. Lin, J. Dehmeshki, G. Slabaugh, G. Beddoe, Shape-based computer-aided detection of lung nodules in thoracic CT images, *IEEE Trans. Biomed. Eng.* 56 (2009) 1810–1820.
- [8] J. Dehmeshki, H. Amin, M. Valdivieso, X. Ye, Segmentation of pulmonary nodules in thoracic CT scans: a region growing approach, *IEEE Trans Med. Imaging* 27 (2008) 467–480.
- [9] A.A. Farag, A. El-Baz, G. Gimel'farb, R. Falk, Detection and recognition of lung abnormalities using deformable templates, in: Proceedings of the 2004 IEEE ICPR, pp. 738–741.
- [10] M. Sofka, C.V. Stewart, Location registration and recognition (LRR) for serial analysis of nodules in lung CT scans, *J. Elsevier Med. Image Anal.* 14 (2010) 407–428.
- [11] S. Taghavi Namin, H. Abrishami Moghadam, R. Jafari, M. Esmail-Zadeh, M. Gity, Automated detection and classification of pulmonary nodules in 3D thoracic CT images, in: Proceedings of the 2010 IEEE SMC Conference, pp. 3774–3779.
- [12] S. Shimoyama, N. Homma, M. Sakai, T. Ishibashi, and M. Yoshizawa, Auto-detection of non-isolated pulmonary nodules connected to the chest walls in X-ray CT images, in: Proceedings of the Conference of 2009 IEEE ICCAS-SICE, pp. 3672–3675.
- [13] S. Lankton, A. Tannenbaum, Localizing region-based active contours, *IEEE Trans. Image Process.* 17 (2008) 2029–2039.
- [14] M. Keshani, Z. Azimifar, R. Boostani, and A. Shakibafar, Lung nodule segmentation using active contour modeling, in: Proceedings of the 2010 IEEE MVIP Conference.
- [15] A. Yezzi, A. Tsai, A. Willsky, A fully global approach to image segmentation via coupled curve evolution equations, *J. Vis. Commun. Image Represent.* 13 (2002) 195–216.
- [16] V. Vapnik, *Statistical Learning Theory*, Wiley, New York, 1998.
- [17] B. Scholkopf, A.J. Smola, *Learning With Kernels*, MIT press, Cambridge, MA, 2002.
- [18] S. Zheng, J. Liu, J.W. Tian, A new efficient SVM-based edge detection method, *J. Elsevier Pattern Recognition Lett.* 25 (2004) 1143–1154.
- [19] B.V. Ginneken, S.G. Armato, B. Hoop, S.V. Amelsvoort-van de Vorst, T. Duindam, M. Niemeijer, K. Murphy, A. Schilham, A. Retico, M.E. Fantacci, N. Camarlinghi, F. Bagagli, L. Gori, T. Hara, H. Fujita, G. Gargano, R. Bellotti, S. Tangaro, L. Bolaos, F.D. Carlo, P. Cerello, S.C. Cheran, E.L. Torres, M. Prokop, Comparing and combining algorithms for computer-aided detection of pulmonary nodules in computed tomography scans: the ANODE09 study, *J. Elsevier Med. Image Anal.* 14 (2010) 707–722.
- [20] < <http://www.via.cornell.edu/databases/lungdb.html> >.
- [21] K. Okada, U. Akdemir, A. Krishnan, Blob segmentation using joint space-intensity likelihood ratio test: application to 3D tumor segmentation, in: Proceedings of the 2005 IEEE CVPR Conference, pp. 437–444.
- [22] R. Bellotti, F.D. Carlo, G. Gargano, S. Tangaro, D. Cascio, E. Catanzariti, P. Cerello, S.C. Cheran, P. Delogu, I.D. Mitri, C. Fulcheri, D. Grosso, A. Retico, S. Squarcia, E. Tommasi, B. Golosio, A CAD system for nodule detection in low-dose lung CTs based on region growing and a new active contour model, *J. Elsevier Med. Phys.* 34 (12) (2007) 4901–4910.
- [23] P. Cerello, S.C. Cheran, F. Bagagli, S. Bagnasco, R. Bellotti, L. Bolanos, E. Catanzariti, G. De Nunzio, E. Fiorina, G. Gargano, G. Gemme, E. Lopez Torres, G. Masala, C. Peroni, M. Santoro, The channeler ant model: object segmentation with virtual ant colonies, in: Proceedings of the IEEE Nucl. Sci. Symp. (2008) 3147–3152.
- [24] A. Retico, F. Bagagli, N. Camarlinghi, C. Carpentieri, M.E. Fantacci, I. Gori, A voxel-based neural approach (VBNA) to identify lung nodules in the ANODE09 study, in: Proc. SPIE 7260 (2009), pp. 72601 S–1–72601 S–8.
- [25] K. Murphy, B. van Ginneken, A.M.R. Schilham, B.J. de Hoop, H.A. Gietema, M. Prokop, A large scale evaluation of automatic pulmonary nodule detection in chest CT using local image features and k-nearest-neighbour classification, *J. Elsevier Med. Image Anal.* 13 (2009) 757–770.
- [26] R. Wiemker, P. Rogalla, T. Blaffert, D. Sifri, O. Hay, E. Shah, R. Truyen, T. Fleiter, Aspects of computer-aided detection (CAD) and volumetry of pulmonary nodules using multislice CT, *Br. J. Radiol.* 78 (2005) S46–S56.
- [27] J. Dehmeshki, X. Ye, X.Y. Lin, M. Valdivieso, H. Amin, Automated detection of lung nodules in CT images using shape-based genetic algorithm, *Comput. Med. Imaging Graph* 31 (2007) 408–417.
- [28] A. Farag, J. Graham, S. Elshazly, A. Farag, Statistical modeling of the lung nodules in low dose computed tomography scans of the chest, in: Proceedings of the 2010 IEEE ICIP, pp. 4281–4284.